Materials Characterization 219 (2025) 114625

Contents lists available at ScienceDirect

Materials Characterization

journal homepage: www.elsevier.com/locate/matchar

# Pore nucleation and growth in aluminium alloy foams analysed by X-ray tomoscopy

K. Georgy [a,*], P.H. Kamm [b], T.R. Neu [b], M. Mukherjee [c], F. García-Moreno [a,b]

[a] Institute of Materials Science and Technology, Technische Universität Berlin, Hardenbergstraße 36, 10623 Berlin, Germany
[b] Institute of Applied Materials, Helmholtz-Zentrum Berlin für Materialien und Energie, Hahn-Meitner Platz 1, 14109 Berlin, Germany
[c] Metal Foams and Porous Materials Lab, Department of Metallurgical and Materials Engineering, Indian Institute of Technology Madras, Chennai 600036, India

ARTICLE INFO

*Keywords:*
Aluminium foam
X-ray
Tomography
Tomoscopy
Nucleation

ABSTRACT

Nucleation and growth of pores in AlSi6Mg4Cu4, AlSi6Cu4, AlCu10, AlSi7 alloys were examined in situ using X-ray tomoscopy. The pore evolution in the foaming precursors was visualized in three dimensions as a function of time. The phases in the alloys were characterised using microscopy. The evolution of the phases with temperature was studied using X-ray tomoscopy. The pore formation was correlated with the temperatures at which different phases formed or evolved. From these studies, the preferred locations for pore initiation were identified. Also, variation in pore size and shape with temperature was studied in detail.

## 1. Introduction

Metal foams have unique properties such as high specific strength, low density and high-energy absorption capability which allow their usage in various commercial applications [1–3]. Even after conducting vast amount of research on metal foams, still it is not easy to reproduce foams with uniform pores, especially for different alloy compositions and production routes. The final pore morphology depends to a large extent on the way pore nucleation takes place. Hence it is imperative to understand the nucleation behaviour of gas pores in metal foams.

Banhart et al. had initially reported that pore formation in metal foams can be of two types: (i) Type I pores, those appearing at the blowing agent site and (ii) Type II pores, those appearing at triple junctions of grains [4]. X-ray radioscopy [5] and X-ray computed tomography (CT) using synchrotron facilities [6–8] have been used already in the early 2000s to understand the pore formation in foams. Helfen et al. studied the foaming of AlSi7 foamable compact with synchrotron microtomography and reported that quantification of pore growth would be possible and changes in pore morphology could be observed [8]. Rack et al. investigated the pore formation in 6061, AlSi6Cu4, and AlSi7 alloy foams and concluded that the melt formation influences pore formation. Although the pores are formed at the location of blowing agents in the case of 6061 alloy, the nucleation in AlSi6Cu4 occurs along the ternary eutectic phase and the pores are generated at the AlSi eutectic in the case of AlSi7 foam [9]. Recently, X-ray tomoscopy has been proposed as a time-resolved method to investigate the metal foaming process (with a spatial resolution up to a few μm and a temporal resolution up to 1 ms) effectively in 3D [10,11]. Also, nucleation in polymer foams has been studied using the same technique [12]. By performing tomoscopy at speeds of 1 tomogram per second, Kamm et al. showed that the nucleation of pores in AlSi8Mg4 foams occurs at the AlMg50 particles [13]. Similar study can be extended to other alloys. The knowledge thus generated on the location of pore formation in different alloy systems would help future studies to gain more control on the uniformity of pore size, e.g., by varying the size, amount and distribution of the particles involved.

Among the alloys studied earlier, only the nucleation behaviour in AlSi8Mg4 was understood clearly, thanks to the tomoscopy technique [13]. In this study, the pore nucleation and growth behaviour of AlSi6Mg4Cu4, AlSi6Cu4, AlCu10, AlSi7 alloys processed via powder metallurgy (PM) route is compared using in-situ X-ray tomoscopy in order to understand the effect of alloy components on the pore nucleation and growth behaviour.

## 2. Experimental

### 2.1. Sample preparation

Al ($D_{50}$ = 64 μm), Si ($D_{50}$ = 27 μm), Cu ($D_{50}$ = 30 μm), AlMg50 ($D_{50}$ = 86 μm) and $TiH_2$ ($D_{50}$ = 14 μm) powders were used for preparing four

* Corresponding author.
*E-mail address:* georgykuriank@gmail.com (K. Georgy).

https://doi.org/10.1016/j.matchar.2024.114625
Received 4 November 2024; Received in revised form 5 December 2024; Accepted 5 December 2024
Available online 8 December 2024

types of representative foamable alloy precursors: AlSi6Mg4Cu4, AlSi6Cu4, AlCu10, AlSi7 (in wt%). $D_{50}$ indicated that 50 % of the particles has diameter smaller than this value. The chemical composition and melting range of the alloys are provided in Table 1. The Al alloy compositions were chosen in such way that the influence of different alloying element (Cu, Mg, Si) on pore nucleation process could be studied and compared. Therefore, Al alloys without Mg (AlSi6Cu4), without Cu (AlSi7), without Si (AlCu10) and including all the elements (AlSi6Mg4Cu4) were chosen for the study. These four alloys were foamed using 0.25 wt% $TiH_2$ as blowing agent, which was preheated in air at 480 °C for 3 h to optimize the gas desorption temperature. In a consolidated precursor, the gas release of $TiH_2$ starts at 343 °C, the first peak of gas release occurs at 579 °C and the maximum (second peak) at 663 °C [14]. The gas release temperatures vary, if the $TiH_2$ powder alone (without considering $TiH_2$ in a compact) is considered. While considering gas release from a $TiH_2$ alone, first onset occurs at 461 °C, second onset occurs at 535 °C and a single peak gas release appears at 647 °C [15].

The precursors were prepared in a 36 mm diameter steel die by two stage powder consolidation (cold compaction for 5 s applying 300 MPa is followed by hot compaction applying 300 MPa at 400 °C for 15 min). Further, 4 mm × 4 mm × 2 mm samples were milled out from the compacted cylindrical precursor for tomoscopy analysis. Even though the original precursor (hot compact with relative density higher than 98 %) is sintered well, they will have few porosities. Hence, it cannot be referred as a porous free sample.

### 2.2. Microscopy

Hot compacted precursors were used for microstructural characterisation performed at room temperature. The precursors were mechanically polished using abrasive papers of various grit sizes in order to achieve mirror finish. The polished precursors were examined using Zeiss Axiophot2 optical microscope and Zeiss crossbeam 340 scanning electron microscope (SEM). The Energy Dispersive X-ray analysis (EDAX) was performed using Bruker XFlash® 6-100. SEM images were picturised using secondary electrons.

### 2.3. X-ray tomoscopy

The experiments were carried out at the TOmographic Microscopy and Coherent rAdiology experimenTs (TOMCAT) beamline, Paul Scherrer Institute (PSI), Switzerland. The tomoscopy set up shown in Fig. 1 was used for acquiring tomograms during foaming of the sample placed within a Boron Nitride (BN) crucible which was mounted on a high-speed rotating stage, as described in the literature [10]. Tomograms with a voxel size of 2.75 μm × 2.75 μm × 2.75 μm composed of 400 projections each were acquired at a speed of 1 tomogram per second during a period of 125 s. Two near Infrared (IR) lasers (150 W each) were used for heating up the samples up to the foaming temperature. The temperature of the samples was tracked by an IR pyrometer pointing to the BN crucible surface and calibrated using a rotating thermocouple, which was close to the bottom portion of the sample. The transmitted X-ray intensities were converted into visible images by using a 150 μm-thick LuAG:Ce scintillator. The magnified images (magnification performed by using a macroscope) were recorded using the GigaFrost high-speed camera [18]. The recorded data was reconstructed using the ASTRA-Toolbox [19] or the gridrec algorithm [20].

**Table 1**
Chemical composition and melting range of alloys used in this study.

| Alloys | Chemical composition | Melting range (°C) | Reference |
|---|---|---|---|
| AlSi6Mg4Cu4 | 6 wt% Si, 4 wt%Mg, 4 wt% Cu, remaining Al | 507– 596 | [16] |
| AlSi6Cu4 | 6 wt% Si, 4 wt% Cu, remaining Al | 525– 612 | [16] |
| AlCu10 | 10 wt% Cu, remaining Al | 548– 630 | [17] |
| AlSi7 | 7 wt% Si, remaining Al | 577– 620 | [8] |

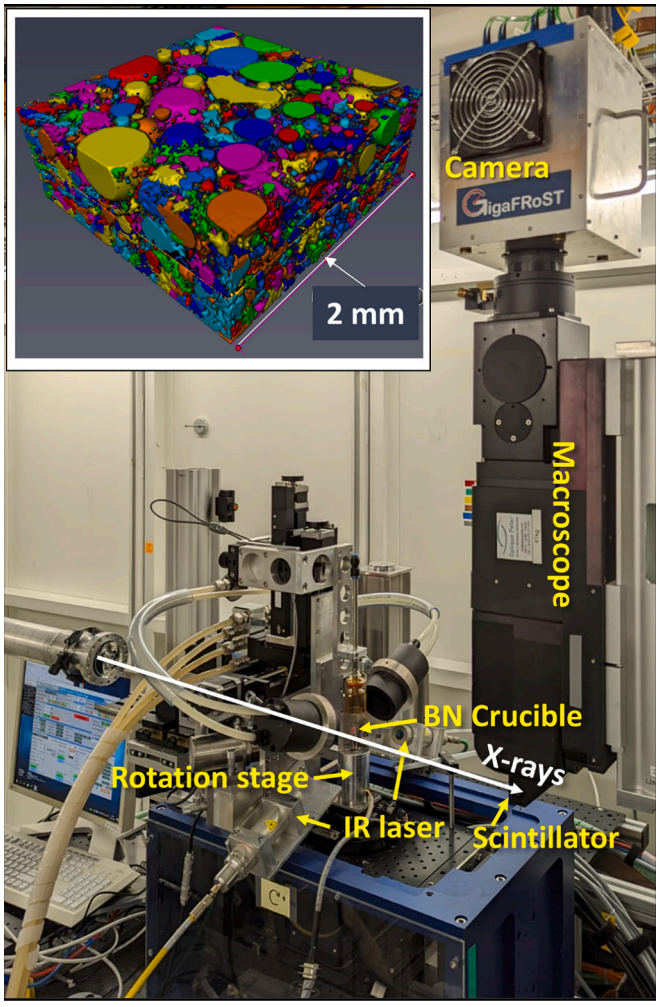


**Fig. 1.** Schematic of the X-ray tomoscopy setup at TOMCAT beamline of Swiss Light Source at PSI. The sample is mounted on a rotation stage and heated inside a BN crucible using two IR lasers. The transmitted X-ray intensities are transformed into visible light using a scintillator and then the macroscope transmits as well as magnifies the visible light into the camera. The inset figure shows an example of a rendered tomogram of an AlSi6Cu4 liquid metal foam at a foaming time of 120 s. Here, the Al matrix is set to be transparent and the segmented pores are shown using random colours (for better visibility).

### 2.4. Image processing

The analysis of the reconstructed tomographic images was performed by executing scripts in MATLAB to quantify pore density (number of pores per unit volume), porosity and sphericity. From the tomograms, square shaped sections (with same dimension for all the alloys) were taken for analysis in order to eliminate the artefacts at the boundaries. Median filter and morphological filters were used to improve the data and watershed segmentation was used to separate the pores in the advanced foaming stages. The noise in the number of pores data was smooth filtered using Savitzky-Golay method with a polynomial order of 3 and a window size of 10 s. Porosity is calculated as the ratio of volume of pores with that of volume of observed region. Equivalent pore diameter of a pore is estimated as the diameter of a sphere having similar volume as that of pore volume. Sphericity of the pores is given by the ratio of projected area of sphere and projected area

of ellipsoid having similar pore volume. The term pore size and pore shape used in this work refers to equivalent pore diameter and sphericity of pores, respectively. In fact, pores nucleate at very small sizes much smaller than detectable by our imaging technique. However, in this work, pores that have grown at least several micrometre (~10 μm) in size are detectable and only such pores are considered as pore nucleation. In this way, although there is a time delay in detection of nucleation, this approximation does not affect the main conclusions of this study since the growing nuclei are always detected at their original location after they reach the detectable limit. Identifying the location of the pore nucleation is the main focus of the present study. The rendered tomogram given in the inset of Fig. 1 was obtained using Avizo software. Fiji software was also used for visualising the tomograms.

## 3. Results

### 3.1. Microstructural characterisation

Optical and SEM images shown in Fig. 2(a)-2(h) reveal the particles/phases present in the compacted alloy precursors at room temperature before foaming. From Fig. 2(b), Fig. 2(d), Fig. 2(f) it can be observed that in the alloys AlSi6Mg4Cu4, AlSi6Cu4, and AlCu10, the Cu particles have an outer layer of Al—Cu compound around them (refer to **Fig. S1** and **Fig. S2** in supplementary material). This outer layer has at least 50 wt% of Cu. A closer SEM examination of these Cu particles shows a further inter diffusion zone of ~10–15 μm depth, by which the Al content vanishes gradually (refer to **Fig. S2** in supplementary material). The microstructure of the AlSi6Mg4Cu4 alloy reveals the presence of β-$Al_3Mg_2$ and γ-$Al_{12}Mg_{17}$ phases present in AlMg50 powders (refer to **Fig. S3** in supplementary material, which shows the point EDAX results for AlMg50 powder). Silicon based oxides are observed in AlSi6Mg4Cu4, AlSi6Cu4 and AlSi7 precursors (refer to Fig. 2(b), Fig. 2(d), Fig. 2(h)). This has been further confirmed by point EDAX and SEM elemental mapping (refer to **Fig. S3** and **Fig. S4** in supplementary material). All precursors also exhibit voids, as observed in Fig. 2(c), Fig. 2(e) and Fig. 2(g). Mg-Si phase was detected in AlSi6Mg4Cu4 and its point EDAX results are provided in **Fig. S5** and **Fig. S6** (in supplementary material).

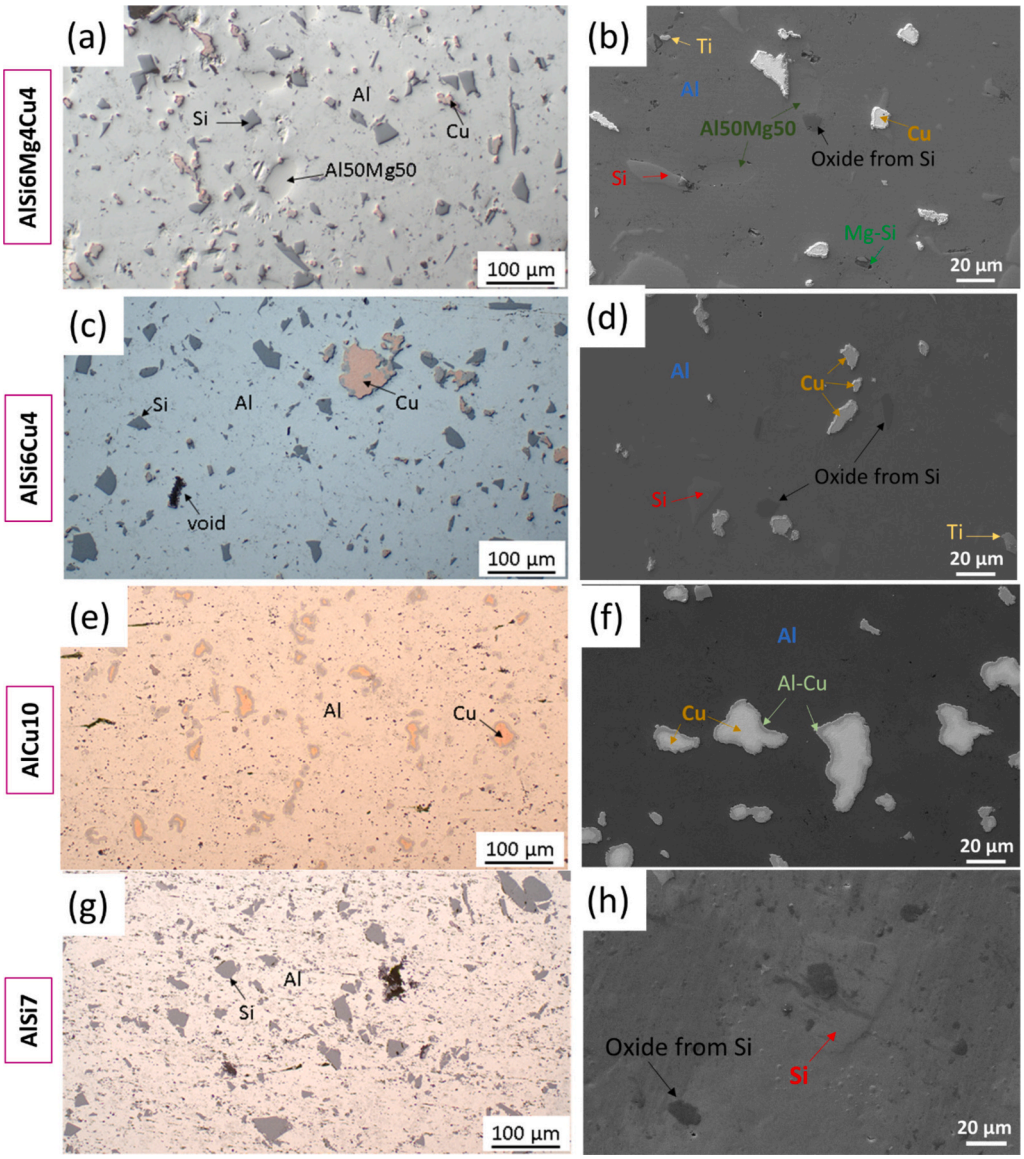


**Fig. 2.** (a), (c), (e), (g) Optical microscopic and (b), (d), (f), (h) SEM images of the consolidated AlSi6Mg4Cu4, AlSi6Cu4, AlCu10 and AlSi7 precursors, respectively showing different phases/particles and voids present at room temperature.

### 3.2. Macrostructural characterisation

Reconstructed slices extracted from tomograms shown in Fig. 3 reveal the phases present during foaming the hot compacted samples. For better understanding, the tomograms obtained are presented with slight contrast adjustments. The structural feature evolution of the AlSi6Mg4Cu4, AlSi6Cu4, AlCu10, AlSi7 alloy precursors at different times ($t_0$, $t_1$, $t_2$, $t_3$) and temperatures during pore nucleation are provided respectively in Fig. 3(a)-3(d), Fig. 3(e)-3(h), Fig. 3(i)-3(l), and Fig. 3(m)-3(p). $t_0$ refers to the time at which the original precursor has not yet begun to melt. $t_1$, $t_2$ and $t_3$ refer to the time corresponding to porosity values of 1 %, 2 % and 3 %, respectively. These porosity values are obtained from the quantitative analysis of the tomograms. Surprisingly, in Fig. 3 pore formation in all the alloys is observed (for example, at time $t_2$ in Fig. 3) below their respective solidus temperatures. **Fig. S7**, **Fig. S8**, **Fig. S9** and **Fig. S10** are provided in supplementary material to demonstrate the pore nucleating regions in a better manner.

In the reconstructed tomographic slices, high X-ray absorbing particles appear brighter (for example, Cu) and low X-ray absorbing particles appear darker (for example Al, AlMg, and Si). The darker Al particles of AlSi6Mg4Cu4 alloy highlighted in Fig. 3(a)-3(c) by a blue oval later act as the source for pore formation in Fig. 3(d). Also, it was observed that large pores appear (on dark AlMg50 particles) at the boundary regions (marked using green oval in Fig. 3(d)). The number of dark particles in AlSi6Mg4Cu4 is higher than in the other alloys.

AlSi6Cu4 shown in Fig. 3(f)-3(h) has a few small black spots representing first gas nuclei and fewer and less dark particles compared to AlSi6Mg4Cu4. Some of the Cu particles (recognized as white bright spots in the tomographic slices) disappear from the Al matrix with shift in time from $t_0$ to $t_1$, which becomes obvious by comparing Fig. 3(e) with Fig. 3(f). At time $t_3$, most of the Cu particles vanish in Fig. 3(h). At the same time, an increased amount of gas nuclei (small black spots) can be observed.

Fig. 3(i) shows the presence of a few dark particles in AlCu10, similar to the ones found in AlSi6Mg4Cu4 (refer to Fig. 3(a)) and AlSi6Cu4 (refer to Fig. 3(e)), highlighted with a blue oval. But in Fig. 3(j), the particle appearance becomes slightly brighter at $t_1$ and finally at $t_3$ (refer to Fig. 3(l)) many nucleation centers appear at their position. Similar bright particles (in blue oval) are observed at $t_1$ in AlSi6Cu4 and AlCu10 alloys (refer to Fig. 3(f) and Fig. 3(j)).

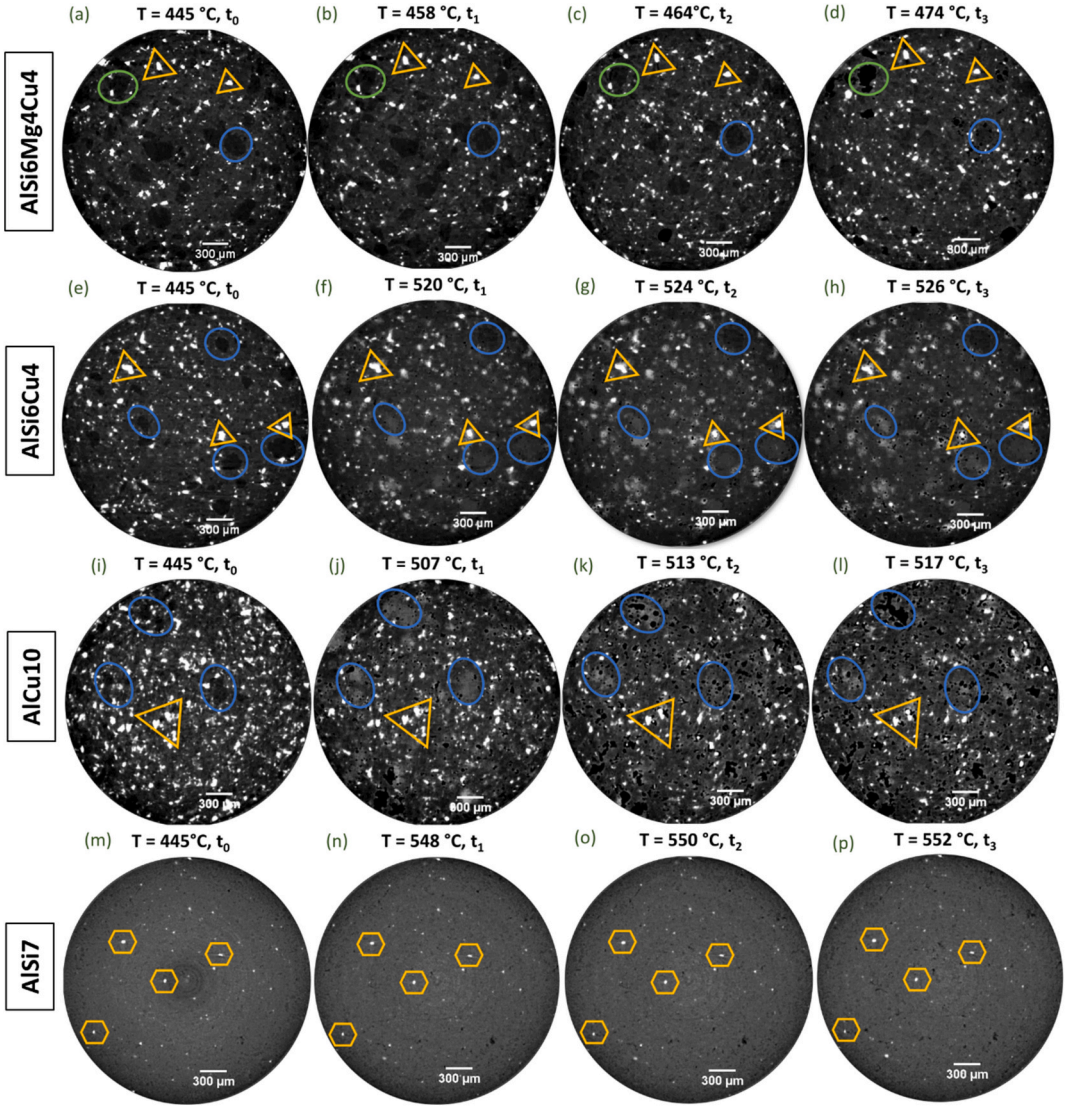


**Fig. 3.** (a)-(d), (e)-(h), (i)-(l), (m)-(p) show the reconstructed tomographic slices of alloys at times $t_0$, $t_1$, $t_2$, $t_3$ and the corresponding temperature (T). The orange triangles show the Cu particles used for tracking the position of the slices in the volume. The green oval in (a)-(d) shows the transition of AlMg50 particles into larger pores. The blue ovals in (e) and (i) show few specific Al particles, and the pore nucleation at the Al particle is shown in (f)-(h) as well as in (j)-(l), respectively. The orange hexagons in (n)-(p) show the tracking of $TiH_2$ particles.

Fig. 3(n)-3(p) shows the formation of random small pores in AlSi7 alloy. Eventhough the AlSi7 alloy contains Si particles (as observed in Fig. 2(g) and Fig. 2(h)), they are not exclusively visible in the tomograms because of the similar X-ray absorption coeficients of Al and Si. The same is true for AlSi6Mg4Cu4 and AlSi6Cu4 alloys. Since Cu and $TiH_2$ have similar appearance (bright contrast) in the tomograms, it is also difficult to distinguish them in AlSi6Mg4Cu4, AlSi6Cu4, and AlCu10 alloys. However, Cu particles can be identified because they are larger than $TiH_2$ and during foaming the contrast of Cu reduces as it diffuses into the matrix unlike the contrast of $TiH_2$ particles which remain unchanged.

Fig. 4 shows comparison of the nucleation steps for AlSi6Mg4Cu4 and AlSi6Cu4 at temperatures different than that mentioned in Fig. 3. In Fig. 4(a)-4(c) we can observe two kinds of nucleation modes in AlSi6Mg4Cu4: (i) large single pores form at the darker particles corresponding to AlMg50 particles, highlighted with green ovals in Fig. 4(b), and (ii) pores are appearing gradually on the dark Al particles (blue ovals in Fig. 4(b)). Fig. 4(d)-4(f) show how the Cu particles (marked as orange triangles in Fig. 4(d)) in AlSi6Cu4 alloy partially disappear in Fig. 4(e) and Fig. 4(f).

Our experiments reveal that in the AlSi6Cu4 alloy (refer Fig. 4(d)-4(f)) some of the pores nucleate at the ring/outer portion of brighter regions, i.e. Cu-enriched regions. Other pores nucleate on the periphery of the dark particles, i.e. Al particles (indicated using an arrow within a black trapezium in Fig. 4(d)). Fig. 5(a)-5(c) show the sudden (within few seconds) formation of large pores in the case of AlSi6Mg4Cu4 alloy. Fig. 5(e)-5(f) show the irregular or crack-like pore in AlSi7 and the generation of pores are at random locations without preferring any specific nucleation sites.

Fig. 6 illustrates the pore evolution with temperature and time. Among the alloys, the pore size is largest in the initial time point (with lowest temperature of 524 °C) for the AlSi6Mg4Cu4 alloy (refer Fig. 6(a), 6(d), 6(g), 6(j)). For all the alloys, with increase in temperature (as well as time) some of the pores are getting coalesced into larger pores (top light blue rectangle) as observed in Fig. 6(h)-6(i). Until 3 % porosity, small irregular pores appear in AlSi7 (refer Fig. 3(p)). After 5 % porosity, crack-like pores appear in AlSi7 (refer to Fig. 6(j)-6(l)). Except for AlSi7, in all the other alloys studied here, pores appeared uniformly distributed in all the tomographic slices (entire sample volume) at a certain instant of time or temperature. The pore formation in the AlSi7 alloy does not occur uniformly in the sample volume. For example, at 111 s (refer Fig. 5(e) and Fig. 6(k)), two types of tomographic slices (at different sections of same sample) are observed in AlSi7. But for other alloys at a certain time or temperature, similar tomographic slices are observed throughout the volume.

### 3.3. Evolution of porous structure

#### 3.3.1. Pore density and porosity

Fig. 7(a) shows pore density and sample temperature during foaming as a function of time. Pores appear first in AlSi6Mg4Cu4 alloy followed by AlSi6Cu4, AlCu10, and AlSi7 alloy. AlSi6Mg4Cu4 has a two-stage nucleation with the nucleation peaks appearing at 43 s and 80 s. Even though pores nucleate early in AlSi6Mg4Cu4 alloy, the maximum pore density in this alloy is lower compared to the same in other alloys. The first peak of the pore density in AlSi6Cu4 occurs after 71 s at around 520 °C and the number of pores decreases slightly at 74 s before creating a second peak at 81 s. AlCu10 has a shoulder at 68 s and a high amount of nucleation spots at around 76 s (refer Fig. 6(g) and Fig. 7(a)) in comparison with other alloys (refer Fig. 6(a), 6(d), 6(j)). Pore nucleation in the AlSi7 alloy starts at a later stage (~77 s) and peaks at 107 s at 591 °C.

Porosity in the AlSi6Mg4Cu4 alloy increases slowly until 550 °C (refer to Fig. 7(b)), but then increases as fast as in the AlSi6Cu4 alloy. From Fig. 7(b), the porosity is highest in AlSi6Mg4Cu4 and lowest in AlSi7 alloy. At the end of foaming process, the porosity of AlCu10 and AlSi7 is almost similar.

#### 3.3.2. Size and shape of pores

The growth of pores in the alloys can be interpreted from the plots presented in Fig. 8. The presence of larger pores in the AlSi6Mg4Cu4

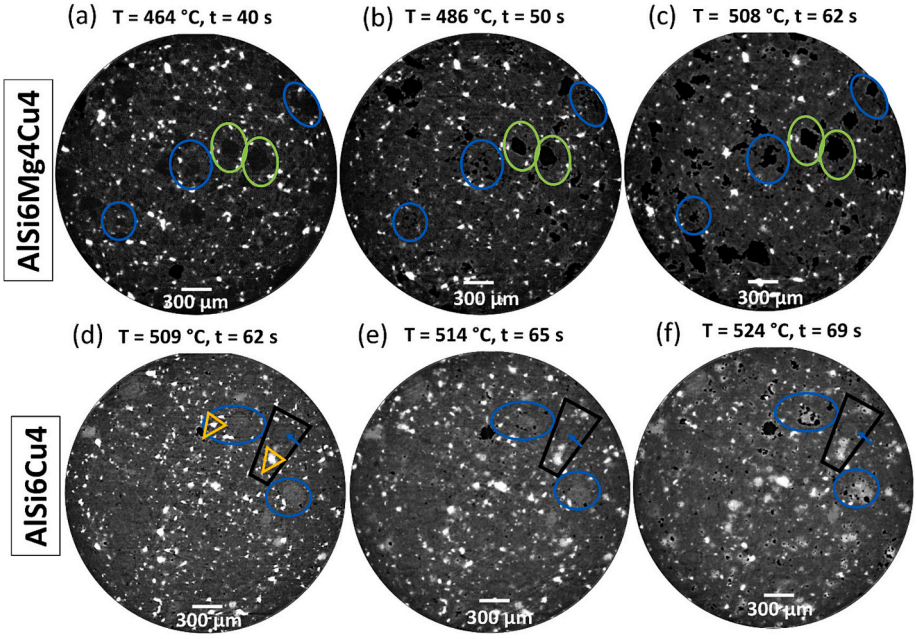


**Fig. 4.** Reconstructed tomographic slices of AlSi6Mg4Cu4 and AlSi6Cu4 alloys and temperature of the samples subjected to foaming with the corresponding time at which the tomograms were acquired. Green ovals in (a)-(c) show pore nucleation at AlMg50 particles and blue ovals in (a)-(c) show the pore formation at Al particles. The black trapezium region in (d)-(f) show Cu particles which easily diffuse into the matrix, but struggles to diffuse into an Al particle (indicated using arrow). The blue ovals in (d)-(f) show diffusion of Cu into adjacent Al particles resulting in pore formation. The orange triangles in (d) show Cu particles. Fig. 4(a) and Fig. 4(f) are the same as Fig. 3(c) and Fig. 3(g), respectively, but shown here again for a better comparison of the pore evolution. (For interpretation of the references to colour in this figure legend, the reader is referred to the web version of this article.)

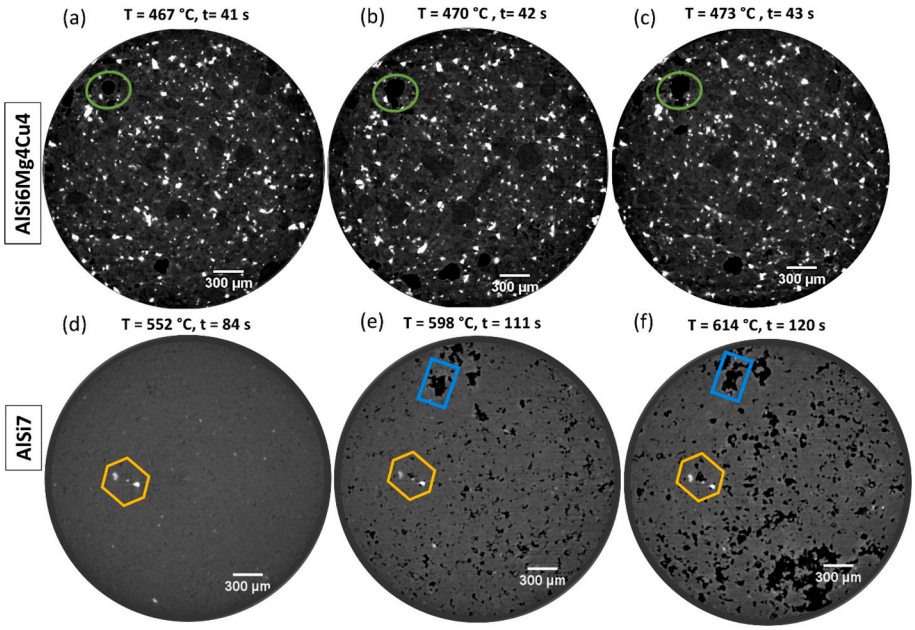


**Fig. 5.** (a)-(c) Kinetics of pore formation in AlSi6Mg4Cu4 alloy and (d)-(f) pore growth in AlSi7. (a)-(c) show the pore evolution for three instances (in steps of 1 s) in between $t_2$ and $t_3$ shown in Fig. 3(c) and 3(d). Green oval in (a)-(c) shows the pore formation from a dark contrast particle. Light blue rectangles in the figures show the pore evolution occurring at different temperatures. Orange hexagons in (d)-(f) show the $TiH_2$ particles used for tracking.

alloy during the early stages of foaming (e.g., up to 75 s) is clearly visible when Fig. 8(a) is compared with Fig. 8(c), Fig. 8(e) and Fig. 8(g). The same is also visible from the tomograms shown in Fig. 6. In all the alloys, the equivalent pore diameter increases with time/temperature. A stepped increase in equivalent pore diameter over time is observed for all the alloys. The first step in AlSi6Mg4Cu4, AlSi6Cu4, AlCu10, and AlSi7 alloys initiates at 30 s, 38 s, 50 s and 78 s, respectively. For AlSi6Mg4Cu4, AlSi6Cu4, AlCu10, and AlSi7 alloys, a region of constant diameter is observed from 50 s to 80 s, 38 s to 65 s, 50 s to 70 s, and 78 s to 83 s, respectively. In case of AlSi6Mg4Cu4, AlSi6Cu4 and AlCu10 alloys, a continuous pore evolution occurs from 80 s (sample temperature of 545 °C), 65 s (sample temperature of 514 °C) and 70 s (sample temperature of 524 °C), respectively. In AlSi7 a sharp second step (refer to Fig. 8(g)) is observed at 83 s (at a sample temperature of 550 °C).

Pores of different sphericities were observed with variation in the alloy composition. In Fig. 8(b), Fig. 8(d) and Fig. 8(f) it is seen that the pores formed at early stages have high sphericity at $t_1$ and then the sphericity decreases (after $t_3$) with increasing equivalent pore diameter for all the alloys. The sphericity of the pores of all alloys is very high at around 105 s, except for AlSi7 alloy. Among the alloys studied in this work, pores with lowest sphericity are observed in AlSi7 alloy.

Figs. 8 (b), Fig. 8(d) and Fig. 8(f) show that the sphericity distribution splits into two major populations in the later stage ($t > 100$ s) for all copper-containing alloys. The sphericity branches out at 99 s, 107 s and 120 s in case of AlCu10, AlSi6Cu4 and AlSi6Mg4Cu4 alloys, respectively. First, a higher fraction of spherical bubbles (sphericity ~0.8—0.9) appears in the AlSi6Cu4 alloy from 107 s, at ~591 °C, while the sphericity of the other pores is between 0.35 and 0.6. A few highly spherical pores (sphericity of >0.9) are present in AlCu10 alloy, but the highest fraction of pores has lower sphericity of ~0.4.

## 4. Discussion

### 4.1. Effect of alloy constituents and composition on pore nucleation

In a PM compact, the alloy formation does not occur uniformly. In this work, the solidus temperature of alloys is reported from literature, but it is not necessary that the alloy will melt at the temperature expected, as we mixed the desired alloy composition mostly from elemental or binary alloy powders, i.e. from different constituents.

#### 4.1.1. Effect of alloy constituents

The constituents in the alloy determine the compounds to be formed by increasing the temperature, and the non-reactive constituents or newly formed compounds may act as a location of pore nucleation. For example, the reaction of constituents may result in gas evolution or the reaction product maybe a lower melting eutectic composition leading to a nucleation site for pore formation. While the first pores are nucleating, the alloy formation is usually still not complete. Therefore, the sample can be considered as a sintered precursor with different particles, and the alloy is formed later, during (or at the end of) the foaming process.

All the Al particles do not behave in similar manner. Most of the aluminium powder in the alloys forms the matrix material by dissolving the rest of the constituents leading to α-Al. However, some of them (dark contrast particles, for example, in Fig. 3(a), 3(e), 3(i)) stay longer as pure Al particles most likely protected by their own oxide layer, which might not have ruptured in the course of compaction. The majority of the Al particles and their oxide layer crack during compaction, which is usually the case for most particles in the course of severe mechanical deformation [21,22]. The diffusion coefficients of Cu in Al (at 560 °C) is $2.1 \times 10^{-13}$ $m^2/s$ and Cu in $Al_2O_3$ (at 560 °C) is $1.85 \times 10^{-27}$ $m^2/s$ [23,24]. Therefore, Cu can easily diffuse through Al but not through $Al_2O_3$. Hence, the presence of an unruptured oxide layer prevents Cu diffusion into such Al particles (within black trapezium in Fig. 4(d)-4(f)) thereby rendering them as dark particles while the other Al particles, in which Cu is dissolved, appear brighter (refer Fig. 6(a), 6(g) and 6(h)). So, it could be inferred that the oxide layer on some of the Al particles in the precursor did not rupture during compaction or that new oxides formed on the Al particles during reheating of the compacted precursor protected them [25,26]. The Al particles with ruptured oxide layer will have slightly brighter contrast compared to the matrix because of the interdiffusion of other elements like Cu.

Presence of AlMg50 powders leads to sudden pore formation during the pore nucleation stage (refer to Fig. 5(a)-5(c)) due to their low melting point. The influence of Si could not be tracked effectively. Si was not visible evidently, even in the tomograms of AlSi7 [9]. Also, $TiH_2$

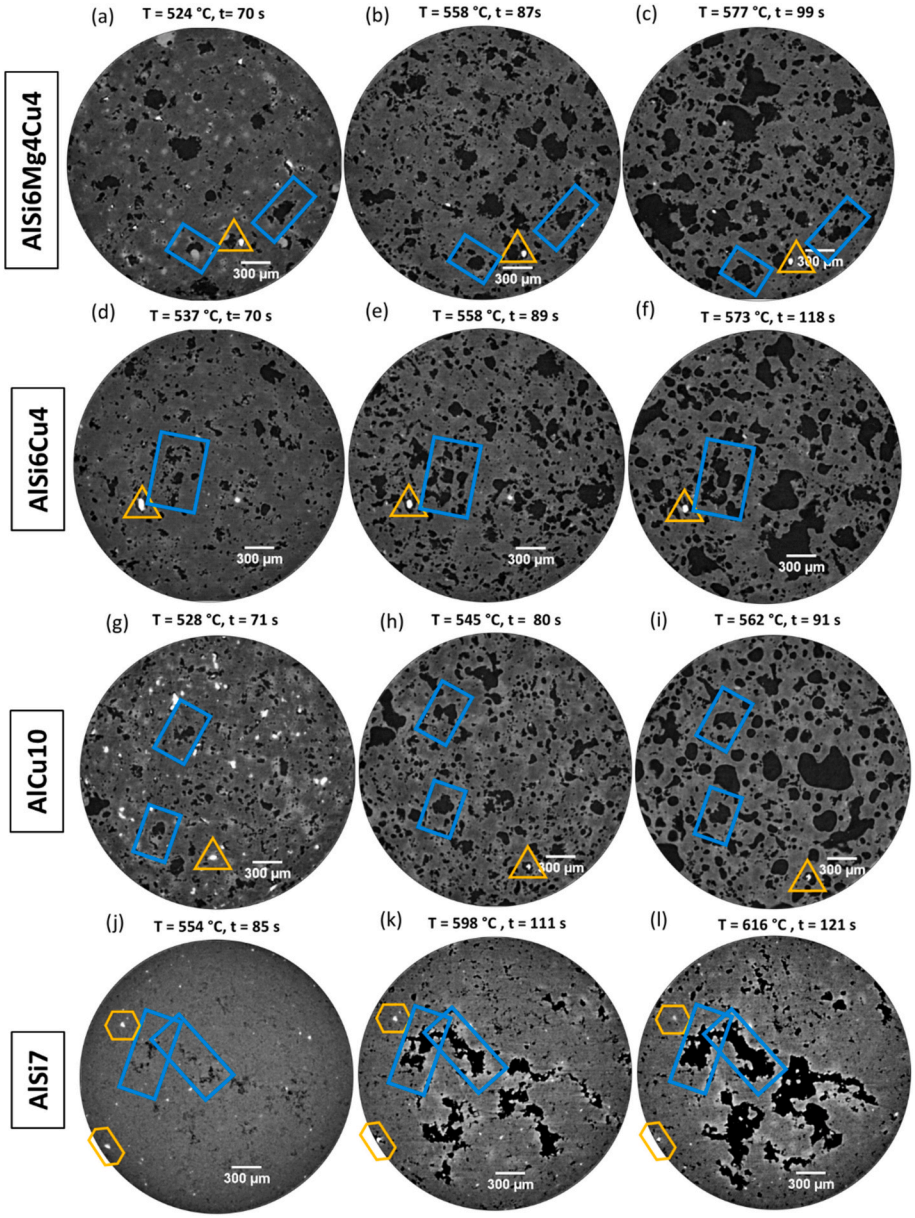


**Fig. 6.** Tomograms of alloy precursors during pore evolution (a)-(c) AlSi6Mg4Cu4, (d)-(f) AlSi6Cu4, (g)-(i) AlCu10 and (j)-(l) AlSi7. For AlSi6Mg4Cu4 and AlSi6Cu4 alloys, the images given above correspond to 10 %, 20 % and 30 % porosities, respectively. For AlCu10 and AlSi7 alloys, the images given above correspond to 5 %, 10 % and 15 % porosities, respectively. Light blue rectangles in the figures show the pore evolution occurring at different porosities. Orange triangles in (a-i) and orange hexagons in (j)-(l) shows the $TiH_2$ particles used also for tracking. (For interpretation of the references to colour in this figure legend, the reader is referred to the web version of this article.)

plays a role in pore nucleation, but less as a reacting constituent than as gas source. It is difficult to observe $TiH_2$ in early stages in Cu containing alloys because both having a similar appearance. In most cases pores don't nucleate at the solid $TiH_2$ particles, although in the course of pore growth they keep trapped at cell walls and stay feeding the pores [4,9].

*4.1.2. Effect of alloy composition*

Even if similar constituents are used, depending on the composition, the number of pores and porosities in the foam varies. All the Cu particles present in the alloys (except AlSi7 alloy) were found to have an Al—Cu layer (refer to Figs. 2(b), 2(d), 2(f)**, Fig. S1, Fig. S2**) formed around them and the thickness was observed to be largest in the AlCu10 alloy. Since 10 wt% of Cu is present in the AlCu10 alloy, pronounced formation of Al—Cu compound around the Cu particles was observed. The Cu concentration around Al particles varies from one particle to another. In the case of AlSi6Cu4 alloy, since the amount of Cu is small (4 wt% or 1.23 vol%), Cu particles are not uniformly distributed. Hence during foaming, the diffusion of Cu into Al particles is not identical for all Al particles, leading to Al—Cu concentration fluctuations of varying composition and consequently varying contrast (refer to Fig. 3(f)-3(h) and Fig. 4(d)-4(f)). However, AlSi6Mg4Cu4 does not show such large contrast variation in Fig. 3, Fig. 4 and Fig. 5, because of the lower sample temperature (temperature mentioned in figure) retarding Cu diffusion. At a higher sample temperature (refer to Fig. 6(a)), the contrast variation is evident in AlSi6Mg4Cu4 and it could be attributed to higher diffusion at higher temperatures.

During foaming (refer to Fig. 4(d)-4(f)), Al particles containing more Cu melt earlier, leading to pore nucleation at the location of these Al particles. At the same time, particles containing less Cu when foaming started, have only sufficient Cu at their outer boundary and start to melt

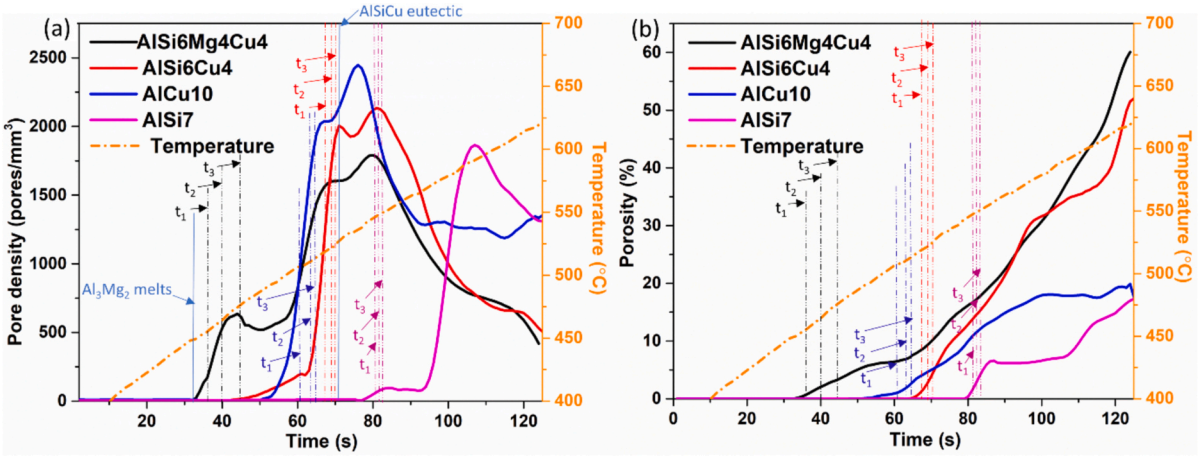


**Fig. 7.** (a) Variation of pore density and temperature as a function of time. (b) Variation of porosity and temperature as a function of time. $t_1$, $t_2$, $t_3$ marked in (a) and (b) correspond to the slices shown in Fig. 3. AlSiCu eutectic formation and melting of AlMg50 (β-$Al_3Mg_2$) are indicated by blue lines in (a). (For interpretation of the references to colour in this figure legend, the reader is referred to the web version of this article.)

only there leading to pore formation. This scenario is enhanced in the case of the AlCu10 alloy because of the high Cu content (refer to **Fig. 3 (j)**). Nucleation is occurring slowest (refer Fig. 7(a)) in the AlSi7 alloy because of their high solidus temperature.

In comparison with the AlSi6Mg4Cu4 alloy, the delayed pore evolution (observed in Fig. 7(a)) in the AlSi6Cu4 alloy can be attributed to a retarded gas release from a single gas source ($TiH_2$, no AlMg50 particles present) [27], a lower liquid fraction at similar temperatures and its higher solidus temperature (solidus temperature of the AlSi6Cu4 alloy and AlSi6Mg4Cu4 is 525 °C and 507 °C, respectively) [14,16,28,29].

### 4.2. *Effect of micro- and macrostructure of alloy on pore nucleation*

#### 4.2.1. *AlSi6Mg4Cu4 alloy*

The nucleation process began at 450 °C in the AlSi6Mg4Cu4 alloy (refer to Fig. 7(a)) and pores appeared at darker regions in Fig. 3(d). Along with the dark contrast of pure Al particles, the presence of 8 wt% AlMg50 powder resulted in large number of dark particles in AlSi6Mg4Cu4 alloy. Some small nucleating pores gradually appeared on pure Al particles (refer to Fig. 4(b)). Other, larger pores rapidly formed (refer to Fig. 5(a)-5(c)) at the melt of low melting phases (β-$Al_3Mg_2$, γ-$Al_{12}Mg_{17}$) in AlMg50 powder. The nucleation started at the melting point of $Al_3Mg_2$ (450 °C) and the initial nucleation peak was observed (at 475 °C) in Fig. 7(b), after the melting of the $Al_{12}Mg_{17}$ (459 °C) phase [13,30]. Pore formation on low melting β-$Al_3Mg_2$ phase (found on the surface of γ-$Al_{12}Mg_{17}$) was previously also observed by Kamm et al. in the case of AlSi8Mg4 alloy, in which AlMg50 powder was used [13]. Hence, in addition to the Type I and Type II pores mentioned by Banhart et al., Type III pores could be coined as the pores appearing at low melting particles/eutectics [4]. The pores appearing at the boundary of the AlSi6Mg4Cu4 sample (refer to Fig. 3d) could be because of the cylindrical heating configuration of the sample resulting in slightly higher temperature (at the sample boundary).

#### 4.2.2. *AlSi6Cu4 alloy*

The dark particles in the AlSi6Cu4 alloy correspond to pure Al (there is no AlMg50 in this composition) particles remaining after the compaction procedure. At time $t_1$, some amount of Cu has already diffused into the Al matrix and hence, some of the Cu particles have disappeared leading to Cu-rich regions (compare Fig. 3(e) and (f)). The increased rate of diffusion at even higher temperatures has led to the disappearance of more Cu particles (refer to Fig. 3(h)). A high delocalized Cu concentration results in many fluctuating lighter bright regions in the matrix.

All the nuclei observed in Fig. 3(f)-Fig. 3(h) are formed near to the regions where AlSiCu eutectic is expected to be present (by correlating with its formation temperature, marked as a vertical dashed blue line in Fig. 7(a)), leading in total to a more homogeneously distributed nucleation. Rack et al. have also reported that the nucleation in AlSi6Cu4 occurs at the ternary eutectic [9]. Therefore, the location of pores is governed by the distribution of the AlSiCu eutectic regions. Also, the Al—Cu compound formed around Cu particles (refer to Fig. 2(c), 2(d), **Fig. S1** in supplementary material) can acts as nucleation point at higher temperatures (Al—Cu eutectic forms at 548 °C) [17].

#### 4.2.3. *AlCu10 alloy*

Similar to the AlSi6Cu4 alloy, the dark particles in the AlCu10 alloy correspond to pure Al particles. The AlCu10 alloy starts melting at its eutectic temperature of 548 °C [17]. Al—Cu compound is formed at the Al/Cu interface as a result of interdiffusion. It is known that in a diffusion couple the low melting point element diffuse faster. Therefore, Al/Cu interface is expected to grow outwards towards the Al matrix, as understood from Kirkendall effect [31].

Guo et al. have reported the presence of compounds such as $Al_4Cu_9$, AlCu, $Al_2Cu$ and further intermetallic phases in diffusion-bonded Cu/Al laminates with an annealing of 10 min at 500 °C [32]. Also, it has been reported that $Al_9Cu_4$ and $Al_2Cu$ are formed at the Al/Cu interface for shorter diffusion times [33]. In the present study also the outer layer of the Cu particle exhibit composition close to the $Al_2Cu$ phase (as observed in **Fig. S2** in the supplementary material). Hence, it could be concluded that an Al—Cu eutectic composition is formed around the Cu particles. Therefore, the weaker low melting eutetic regions lead to the formation of the earliest gas nuclei.

Note that, the dark particles marked in blue ovals (refer to Fig. 3(i)) are pure Al powder particles (Mg is not present in this alloy), which are then massively and sudden infiltrated by Cu (due to diffusion) probably due to the rupture of the protective $Al_2O_3$ layer as can be observed as brighter regions at $t_1$ in Fig. 3(j) [34]. Hence, a considerably high amount of pores appear on the location in which Al particles were present earlier (refer to Fig. 3(j)).

#### 4.2.4. *AlSi7 alloy*

The formation of crack-like pores in the AlSi7 alloy (refer to Fig. 5(f) and Fig. 6(k)) can be attributed to the internal gas pressure created by the blowing agent, which cannot be counteracted by the alloy strength at that high temperature, leading to internal failure. Helfen et al. have mentioned that the pore formation in AlSi7 occurs at the regions around Si particles [6] and similarly Rack et al. reported that the pores are

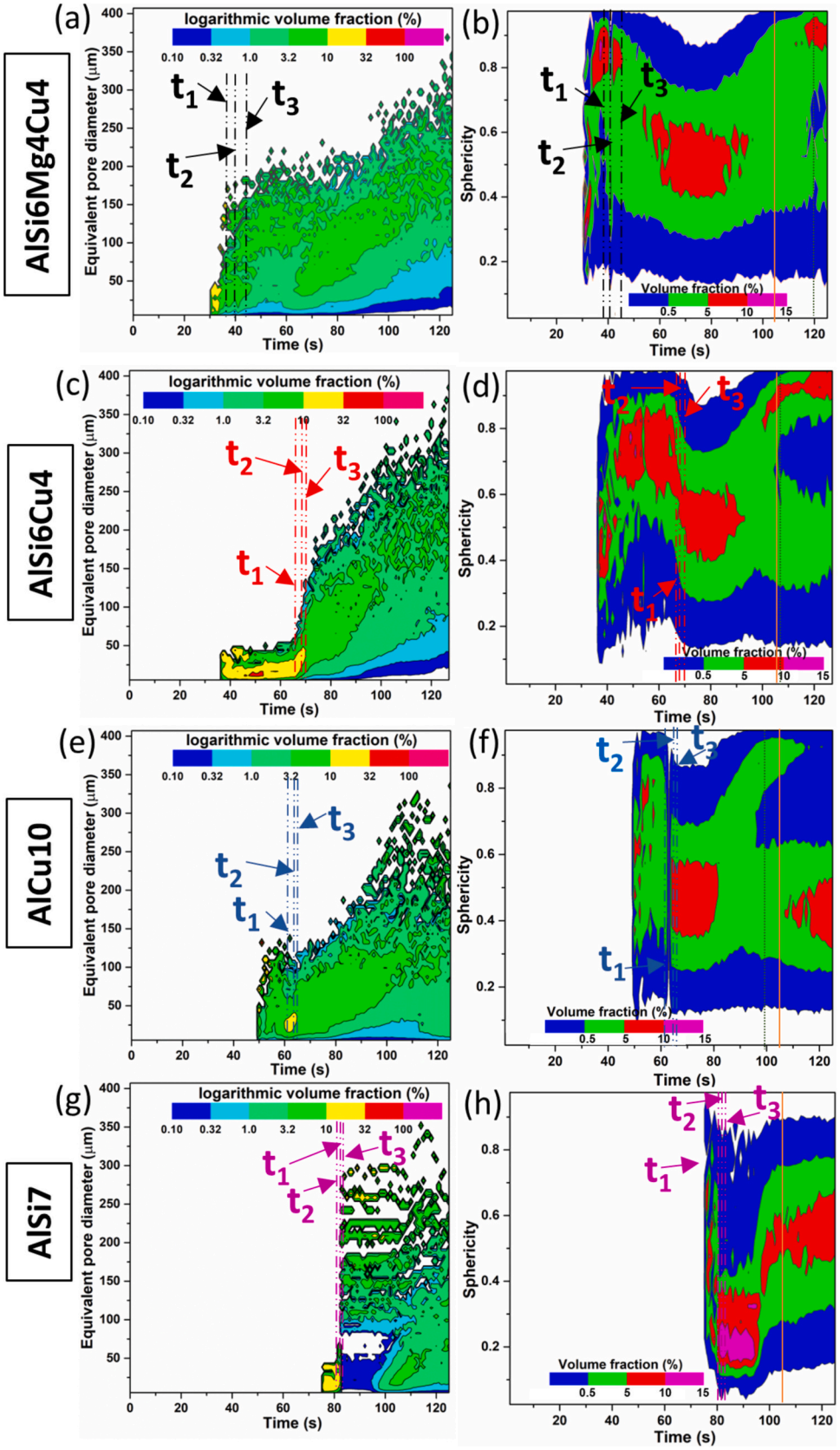


**Fig. 8.** (a), (c), (e), (g) Variation of equivalent pore diameter with volume fraction of pores as a function of time for the different alloys. The colour coding in the inset shows the distribution of logarithmic volume fraction of pores. (b), (d), (f), (h) Variation of sphericity and volume fraction of pores as a function of time. The colour coding shows the distribution of pore volume fraction. $t_1$, $t_2$, $t_3$ correspond to the times mentioned in Fig. 3. Orange colour vertical line at 105 s in (b), (d), (f), (h) indicates large pores with high sphericity. Dotted dark green line at 120 s, 107 s and 99 s for AlSi6Mg4Cu4, AlSi6Cu4, and AlCu10 alloys indicates the time point after which the sphericity population splits up in to two branches.

arising at loosely compacted regions (Al/Si interface) [9].

According to literature, there is a mismatch between the alloy's solidus temperature (577 °C) and the temperature of the initiation of gas release from treated $TiH_2$ (from a powder compact, pre-oxidized $TiH_2$ has a first onset at 343 °C and a first peak at 579 °C followed by a major second peak at 663 °C) [8,14]. This mismatch leads first to increase of the internal pressure at the gas sources, leading to cracks up to the sample surface and consequently a lot of gas losses in the case of AlSi7 alloy, which eventually results in lesser expansion/foaming and sometimes to very large pores generated from the initial inner cracks [8,9].

### 4.3. Effect of pore size, porosity, pore density and pore shape on pore growth

#### 4.3.1. Effect of pore size and porosity

The stepped increase in equivalent pore diameter during foaming (shown in Fig. 8(a), 8(c), 8(e) and Fig. 8(g)) indicates that at a precise temperature new large pores are generated quite fast or existing ones grow at once. Otherwise, if small pores had continued to further grow or merge together, this increase (in pore size) would have been gradual or smoother. In the case of AlSi6Mg4Cu4 alloy, the first step in pore size refers to the pores formed during melting of AlMg50 particles (~ 450 °C), and in the constant diameter region the solidus temperature (507 °C) of the alloy was attained, which eventually leads to continuous pore evolution. The continuous pore evolution in AlSi6Cu4 and AlCu10 initiates (sample temperatures are 514 °C and 524 °C, respectively) near to their solidus temperature of 525 °C and 548 °C, respectively. The second step in AlSi7 (refer Fig. 8(g)) indicates the transition from irregular pores to large crack-like pores. The second step initiates at 550 °C, which is below the solidus temperature (577 °C) of the alloy and hence crack-like pores are appearing.

The rate of liquid phase formation is different for different alloys and depending on that fraction, the pore size distributions vary. For example, AlSi6Mg4Cu4 has higher liquid fraction in the temperature range of 530—600 °C in comparison with that of AlSi6Cu4. The liquid fraction of AlSi6Mg4Cu4, AlSi6Cu4 alloys (at 550 °C, which is at least 25 °C above the solidus temperature of both the alloys) are 48 % and 16 % respectively [16]. The larger equivalent pore diameter in AlSi6Mg4Cu4 within the initial time frame of 38 s to 70 s could be attributed to their high liquid fraction (coupled with presence of low melting AlMg50 particles). The liquid fraction will be the lowest in AlCu10 having a liquidus temperature of 630 °C and the liquid fraction in AlSi7 (a liquidus temperature of 620 °C) is slightly higher than AlCu10 [8,16,17].

Large pores (in high volume fraction) result in higher porosity. AlSi6Mg4Cu4 and AlSi6Cu4 have higher volume fraction of larger pores (pores with size larger than 150 μm). Therefore, by correlating Fig. 8(a), 8(c), 8(e), 8(f) with Fig. 7(b), it can be noted that the porosities of AlSi6Mg4Cu4 and AlSi6Cu4 are higher than that of AlCu10 and AlSi7 alloys. The increase in porosity of the AlSi6Mg4Cu4 alloy (observed in Fig. 7(b)) could be attributed to the combined gas release from $TiH_2$ and AlMg50 (peak gas release of treated $TiH_2$ powder and AlMg50 is at 579 °C and 423 °C, respectively) [15,29]. Lower liquid fraction reduces the amount of porosity in AlCu10 and AlSi7 alloys. Even though AlSi7 alloy exhibits large crack-like pores in some locations (refer Fig. 6(k)), the overall porosity is low (Fig. 7(b)) because most of the sample has lower porosity and plenty of the foaming gas is lost to the surrounding (refer to Fig. 5(e)).

#### 4.3.2. Effect of pore density

The peak in the pore density plot (refer to Fig. 7(a)) for AlSi6Mg4Cu4 and AlSi6Cu4 alloy can be found in the range of 540- 550 °C (above the solidus temperature of the alloys), which is near to the first peak gas release temperature (343 °C is the onset of $TiH_2$ gas release and 579 °C is the first peak of gas evolution from a compact) of the treated $TiH_2$ [15]. The dip in pore density observed for AlSi6Cu4 after the initial nucleation peak at 71 s could be attributed to pore coalescence. Then, the second nucleation peak at 81 s is the result of new pores getting generated. In general, a high number of pores at a certain porosity means a narrower pore distribution and usually a finer porous structure of the resulting metal foam. Maximum pore density in case of the AlCu10 alloy (Fig. 7 (a)) coupled with its low porosity amount (Fig. 7(b)) implies nucleation of small pores, which is evident from Fig. 3(i).

#### 4.3.3. Effect of pore shape

Uniformly distributed small spherical pores are observed in AlSi6Mg4Cu4, AlSi6Cu4 and AlCu10 alloys at the beginning (~50 s) resulting in large sphericity. After some time, there is a drop in sphericity. Pores merge with each other at this stage, which also becomes obvious from the increase in pore size. The merged pores are not able to minimize their surface energy, therefore cannot achieve a high sphericity because at this stage there is hardly any liquid fraction available to enable this [16]. The drop in sphericity is the highest in the case of AlSi7 alloy, which can be attributed to the crack-like pores formed. Later, the sphericity of the pores in AlSi7 and in other alloys improves gradually again due to the availability of a larger liquid fraction at the later stages. Large volume fraction (refer Fig. 8(d)) of highly spherical pores as observed in AlSi6Cu4 initially (40 s to 60 s) is the result of a uniformly distributed pore nucleation. High sphericity at the end of foaming (~105 s) can be attributed to the fact that the alloys have reached their liquidus temperature. Thereafter, the surface tension acting on the pores round them and eventually resulting in spherical bubbles. The branching out of sphericities (observed in Fig. 8(b), 8(d), 8(f)) in AlSi6Mg4Cu4, AlSi6Cu4, and AlCu10 alloys occurs because of the pore collapse occurring at higher temperature/time [35].

### 4.4. Porosity formation below solidus temperature

The solidus temperature of AlSi6Mg4Cu4, AlSi6Cu4, AlCu10, AlSi7 alloys are 507 °C, 525 °C, 548 °C, and 577 °C, respectively, as per the literature [8,16,17]. However, the pore formation was observed in all the alloys (refer to Fig. 3) below their solidus temperature, as the nominal alloy compositions are still not fully formed from the individual constituents at those temperatures and because of the presence of lower melting phases. In AlSi6Mg4Cu4, low melting AlMg50 particles are the location for pore nucleation even before reaching the solidus temperature, because of the presence of low melting β-$Al_3Mg_2$ and/or γ-$Al_{12}Mg_{17}$ phases. Powder compacts are never 100 % dense even after they undergo liquid phase sintering [17]. Therefore the compacts used for the tomoscopy experiments contain few pores in between powder particles [36]. It is known that adsorbates (e.g. water) are present on the powder surface, which are capable of releasing gas (such as $H_2$) even before the decomposition of blowing agent [29]. In fact, heating of well-compacted precursors even without $TiH_2$ to high temperatures, but below their solidus temperatures, can lead to some expansion (pore formation). This expansion is attributed to the adsorbed gases (hydrocarbon, hydroxides), dissolved gases ($N_2$, $O_2$, $H_2O$, $CO_2$, CO) and entrapped gases ($H_2$) [37].

Pre-existing pores can expand by creep mechanism. Ashby has reported that the PM samples having pores comprised of inert gas at high pressure can lead to creep because of further generation of pressure in the pore at higher temperature. As a result, individual pores expand leading to an expansion of the sample. This process has been exploited in Ti alloys for producing pore fraction of 0.5 and pores in the size range of 10—300 μm [38]. The same is also applicable for all the alloy precursors in the present study because compaction was performed at a high pressure (300 MPa).

Mukherjee has also reported that there is an expansion up to 5 % because of the pressure build up generated by early decomposition of $TiH_2$ and adsorbates [39]. Elzey et al. have reported that porosity of ~40 % could be present, even before approaching solidus temperature. In solid state foaming, heat treatment of a compact in which gas is

entrapped between the voids, results in the expansion of gases [40]. Atwater et al. have reported that oxides present on the particles eventually results in steam, that gets expanded in to microscale voids [41].

Duarte et al. commented on the possibility of void formation (near defects) in the solid state, because of the $TiH_2$ decomposition [26]. Lazaro et al. have pointed out that the early expansion is the result of microstructural anisotropy developed during precursor preparation [42,43]. Therefore, it can be concluded that the pore formation observed below the solidus temperature resulted from the expansion of pre-existing pores assisted by the gas evolution from adsorbates and also from AlMg50 powder in the case of AlSi6Mg4Cu4 alloy.

### 4.5. Nucleation mechanism

Based on the microscopy and tomography results, the findings and discussion of the pore nucleation mechanisms in this study are summarized in Fig. 9. With increase in temperature, the dark particles (pure Al or AlMg50 shown in Fig. 9(a), Fig. 9(d) and Fig. 9(g)) transform to bright particles due to the diffusion of alloying elements like Cu building α-Al in Fig. 9(c), Fig. 9(f) and Fig. 9(i). Mostly, the first pores are appearing around these bright regions. But some of the dark pure Al particles do not become bright at the same time even after heating. The pores appearing on these dark particles, pointed on to the fact that the Cu diffusion is hindered by an $Al_2O_3$ layer up to a certain extent. At higher temperatures the interdiffusion of Al and Cu results in the formation of (Al) and (Cu) solid solutions.

## 5. Conclusions

AlSi6Mg4Cu4, AlSi6Cu4, AlCu10 and AlSi7 alloy compacts were prepared and their foaming behaviour was studied in-situ using X-ray tomoscopy. The location of initial pore formation was tracked, which allowed the identification of the regions/particles at which pore nucleation occurs. Nucleation as well as evolution of pores are different and complex in each of the four alloys studied here. The pore nucleation depends on the constituents and composition of the alloy, diffusion of the constituents into each other, and the microstructural phases present. The equivalent pore diameter as well as the sphericity of the pores

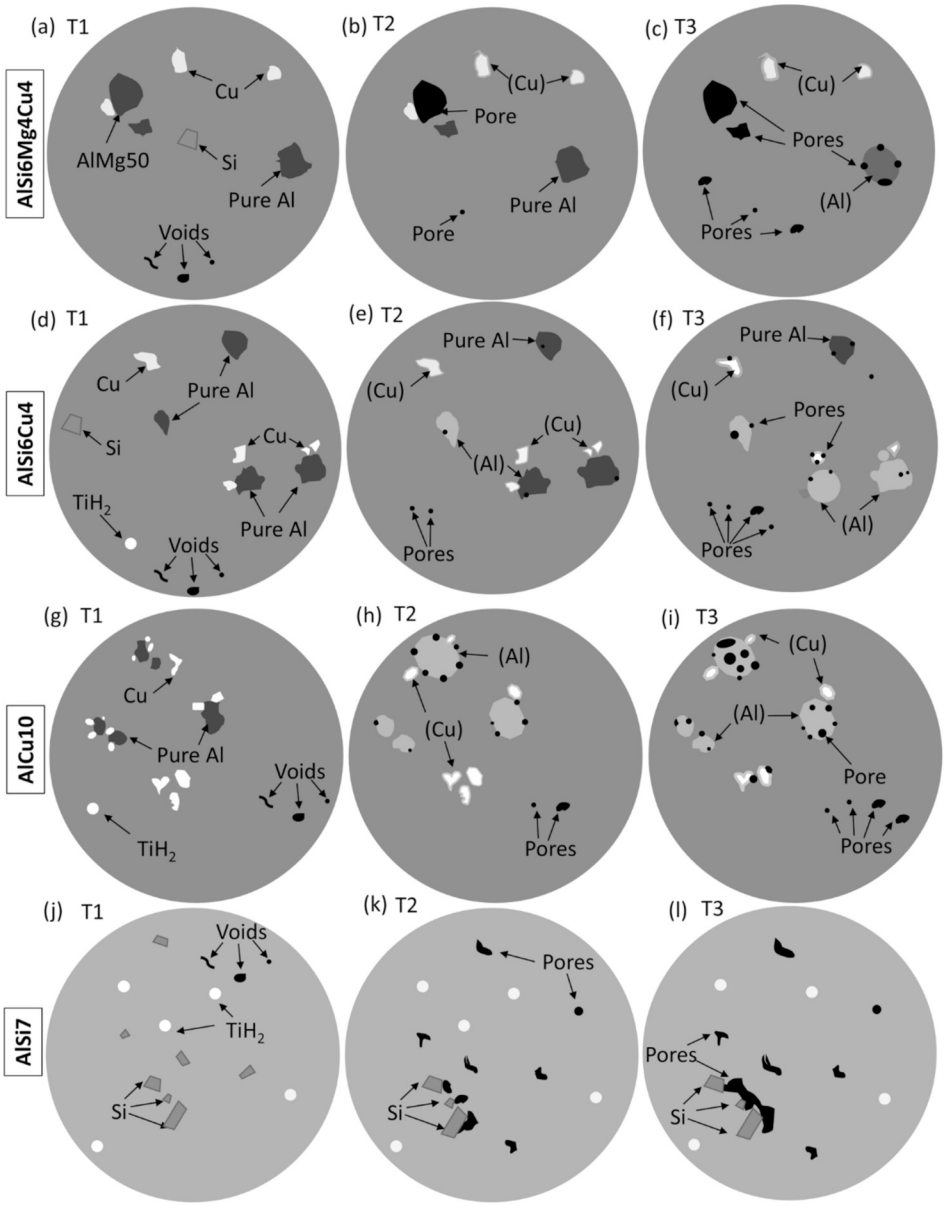


**Fig. 9.** Illustration of nucleation and growth of pores in the alloys. (a-c) AlSi6Mg4Cu4 alloy, (d-f) AlSi6Cu4 alloy, (g-i) AlCu10 alloy and (j-l) AlSi7 alloy. (Al) and (Cu) indicate solid solutions of Al and Cu, respectively. The changes in the alloy with increase in temperature during nucleation (T3 > T2 > T1) is shown.

depend mainly on the nucleation modes, melting temperature of the alloy and its constituents, and the liquid fraction available at a given temperature.

The outputs of the work are summarized in the subsequent points.

- For all the alloys, the first nucleation of pores occurs before solidus temperature because of the expansion of the pre-existing voids in PM precursors. These pre-existing voids expand either or both by a creep mechanism when the metallic matrix become soft at elevated temperature and due to a high internal gas pressure by the release of the adsorbed gases from the surface of metal powders. The other subsequent pore nucleation mechanisms for each alloy are mentioned below.
- The nucleation in AlSi6Mg4Cu4 occurs mainly in three steps and places: (a) large pores form faster on lower melting AlMg50 particles, (b) small pores nucleate then on Cu-rich Al (former pure Al) particles and (c) pores also appear on Cu-rich α-Al particles all over the matrix.
- The nucleation in AlSi6Cu4 occurs in two places: (a) some of the pores form at the Cu-rich Al (former pure Al) particles and (b) some pores form at Al-Si-Cu eutectic regions.
- In the case of AlCu10 alloy, the nucleation also takes place in two places: (a) small pores nucleate at Cu-rich (former pure Al) particles and (b) other pores are homogenously distributed at Cu-rich α-Al matrix regions in the periphery of Cu particles.
- Foams made of AlSi7 alloy have crack-like pore nucleation, probably at Al/Si interfaces.

## CRediT authorship contribution statement

**K. Georgy:** Writing – review & editing, Writing – original draft, Visualization, Validation, Software, Resources, Project administration, Methodology, Investigation, Formal analysis, Data curation, Conceptualization. **P.H. Kamm:** Writing – review & editing, Visualization, Validation, Software, Resources, Project administration, Methodology, Investigation, Formal analysis, Data curation, Conceptualization. **T.R. Neu:** Writing – review & editing, Visualization, Validation, Supervision, Software, Resources, Methodology, Investigation, Formal analysis, Data curation, Conceptualization. **M. Mukherjee:** Writing – review & editing, Visualization, Validation, Supervision, Software, Resources, Data curation, Conceptualization. **F. García-Moreno:** Writing – review & editing, Writing – original draft, Visualization, Validation, Supervision, Software, Resources, Project administration, Methodology, Investigation, Funding acquisition, Formal analysis, Data curation, Conceptualization.

## Declaration of competing interest

The authors declare that they have no known competing financial interests or personal relationships that could have appeared to influence the work reported in this paper.

## Data availability

Data will be made available on request.

## Acknowledgements

We are thankful to H. Kropf for helping with the SEM analysis and Ch. Förster for sample preparation. The authors gratefully acknowledge financial support through the DFG Reinhart-Koselleck Project 408321454, Ba 1170/40, and BMBF Award 05K18KTA. We acknowledge the Paul Scherrer Institute, Villigen, Switzerland, for the provision of synchrotron radiation beamtime at the TOMCAT beamline X02DA of the SLS.

## Appendix A. Supplementary data

Supplementary data to this article can be found online at https://doi.org/10.1016/j.matchar.2024.114625.

## References

[1] F. García-Moreno, Commercial applications of metal foams: their properties and production, Materials 9 (2016) 20–24, https://doi.org/10.3390/ma9020085.
[2] B.J. Marx, A. Rabiei, Overview of composite metal foams and their properties and performance, Adv. Eng. Mater. 19 (2017) 1–13, https://doi.org/10.1002/adem.201600776.
[3] B. Parveez, N.A. Jamal, H. Anuar, Y. Ahmad, A. Aabid, M. Baig, Microstructure and mechanical properties of metal foams fabricated via melt foaming and powder metallurgy technique, Materials 15 (2022) 5302, https://doi.org/10.3390/ma15155302.
[4] J. Banhart, D. Bellmann, H. Clemens, Investigation of metal foam formation by microscopy and ultra small-angle neutron scattering, Acta Mater. 49 (2001) 3409–3420, https://doi.org/10.1016/S1359-6454(01)00256-7.
[5] F. Garcia-Moreno, M. Mukherjee, C. Jiménez, A. Rack, J. Banhart, Metal foaming investigated by X-ray radioscopy, Metals 2 (2011) 10–21, https://doi.org/10.3390/met2010010.
[6] L. Helfen, T. Baumbach, P. Pernot, P. Cloetens, H. Stanzick, K. Schladitz, J. Banhart, Investigation of pore initiation in metal foams by synchrotron-radiation tomography, Appl. Phys. Lett. 86 (2005) 1–3, https://doi.org/10.1063/1.1941453.
[7] J. Banhart, H. Stanzick, L. Helfen, T. Baumbach, Metal foam evolution studied by synchrotron radioscopy, Appl. Phys. Lett. 78 (2001) 1152–1154, https://doi.org/10.1063/1.1350422.
[8] L. Helfen, T. Baumbach, H. Stanzick, J. Banhart, A. Elmoutaouakkil, P. Cloetens, Viewing the early stage of metal foam formation by computed tomography using synchrotron radiation, Adv. Eng. Mater. 4 (2002) 808–813, https://doi.org/10.1002/1527-2648(20021014)4:10<808::AID-ADEM808>3.0.CO;2-U.
[9] A. Rack, H.M. Helwig, A. Bütow, A. Rueda, B. Matijašević-Lux, L. Helfen, J. Goebbels, J. Banhart, Early pore formation in aluminium foams studied by synchrotron-based microtomography and 3-D image analysis, Acta Mater. 57 (2009) 4809–4821, https://doi.org/10.1016/j.actamat.2009.06.045.
[10] F. García-Moreno, P.H. Kamm, T.R. Neu, F. Bülk, R. Mokso, C.M. Schlepütz, M. Stampanoni, J. Banhart, Using X-ray tomoscopy to explore the dynamics of foaming metal, Nat. Commun. 10 (2019) 1–9, https://doi.org/10.1038/s41467-019-11521-1.
[11] F. García-Moreno, P.H. Kamm, T.R. Neu, F. Bülk, M.A. Noack, M. Wegener, N. von der Eltz, C.M. Schlepütz, M. Stampanoni, J. Banhart, Tomoscopy: time-resolved tomography for dynamic processes in materials, Adv. Mater. 33 (2021) 290–291, https://doi.org/10.1002/adma.202104659.
[12] S. Pérez-Tamarit, E. Solórzano, R. Mokso, M.A. Rodríguez-Pérez, In-situ understanding of pore nucleation and growth in polyurethane foams by using real-time synchrotron X-ray tomography, Polymers 166 (2019) 50–54, https://doi.org/10.1016/j.polymer.2019.01.049.
[13] P.H. Kamm, T.R. Neu, F. García-Moreno, J. Banhart, Nucleation and growth of gas bubbles in AlSi8Mg4 foam investigated by X-ray tomoscopy, Acta Mater. 206 (2021) 116583, https://doi.org/10.1016/j.actamat.2020.116583.
[14] C. Jiménez, F. Garcia-Moreno, M. Mukherjee, O. Goerke, J. Banhart, Improvement of aluminium foaming by powder consolidation under vacuum, Scr. Mater. 61 (2009) 552–555, https://doi.org/10.1016/j.scriptamat.2009.05.020.
[15] C. Jiménez, F. Garcia-Moreno, B. Pfretzschner, M. Klaus, M. Wollgarten, I. Zizak, G. Schumacher, M. Tovar, J. Banhart, Decomposition of $TiH_2$ studied in situ by synchrotron X-ray and neutron diffraction, Acta Mater. 59 (2011) 6318–6330, https://doi.org/10.1016/j.actamat.2011.06.042.
[16] H.-M. Helwig, F. Garcia-Moreno, J. Banhart, A study of Mg and Cu additions on the foaming behaviour of Al-Si alloys, J. Mater. Sci. 46 (2011) 5227–5236, https://doi.org/10.1007/s10853-011-5460-5.
[17] G.B. Schaffer, T.B. Sercombe, R.N. Lumley, Liquid phase sintering of aluminium alloys, Mater. Chem. Phys. 67 (2001) 85–91, https://doi.org/10.1016/S0254-0584(00)00424-7.
[18] G. Theidel, H. Billich, E. Schmid, T. Celcer, G. Mikuljan, L. Sala, GigaFRoST: the gigabit fast readout system for tomography research papers, J. Synchrotron Radiat. 24 (2017) 1250–1259, https://doi.org/10.1107/S1600577517013522.
[19] W. Van Aarle, W.J. Palenstijn, J. Cant, E. Janssens, F. Bleichrodt, A. Dabravolski, J. De Beenhouwer, K.J. Batenburg, J. Sijbers, Fast and flexible X-ray tomography using the ASTRA toolbox, Opt. Express 24 (2016) 25129–25147, https://doi.org/10.1364/OE.24.025129.
[20] F. Marone, M. Stampanoni, Regridding reconstruction algorithm for real-time tomographic imaging research papers, J. Synchrotron Radiat. 19 (2012) 1029–1037, https://doi.org/10.1107/S0909049512032864.
[21] L.E.G. Cambronero, J.M. Ruiz-Roman, F.A. Corpas, J.M. Ruiz Prieto, Manufacturing of Al-Mg-Si alloy foam using calcium carbonate as foaming agent, J. Mater. Process. Technol. 209 (2009) 1803–1809, https://doi.org/10.1016/j.jmatprotec.2008.04.032.
[22] Y. Lao, H. Du, T. Xiong, Y. Wang, Evolution behaviors of oxides in severely plastic deformed region of AISI 52100 Steel during dry sliding wear, J. Mater. Sci. Technol. 33 (2017) 330–337.
[23] E. Crossin, J.-Y. Yao, G.B. Schaffer, Swelling during liquid phase sintering of Al-Mg-Si-Cu alloys, Powder Metall. 50 (2007) 354–358, https://doi.org/10.1179/174329007X223947.

[24] F. Moya, E.G. Moya, D. Juve, D. Treheux, C. Grattepain, M. Aucouturier, SIMS study of copper diffusion into bulk alumina, Scr. Metall. Mater. 28 (1993) 343–348.
[25] W. Kehl, H.F. Fischmeister, Liquid phase sintering of Al-Cu compacts, Powder Metall. (1980) 113–119, https://doi.org/10.1179/pom.1980.23.3.113.
[26] I. Duarte, J. Banhart, A study of aluminium foam formation-kinetics and microstructure, Acta Mater. 48 (2000) 2349–2362, https://doi.org/10.1016/S1359-6454(00)00020-3.
[27] M. Mukherjee, F. Garcia-Moreno, C. Jiménez, J. Banhart, Al and Zn foams blown by an intrinsic gas source, Adv. Eng. Mater. 12 (2010) 472–477, https://doi.org/10.1002/adem.201000017.
[28] X. Ding, B. Peng, X. Hu, K. Pan, Y. Liu, T. Wan, S. Ran, Effect of Cu and Sn additions on the cellular structure of Al-Si-Mg alloys foaming at low temperature (≤ 600 °C), Composites Part B. 234 (2022) 109693, https://doi.org/10.1016/j.compositesb.2022.109693.
[29] C. Jiménez, F. Garcia-Moreno, J. Banhart, G. Zehl, Effect of relative humidity on pressure-induced foaming (PIF) of aluminium-based precursors, in: 5th International Conference on Porous Metals and Metallic Foams, 2008, pp. 59–62.
[30] J.L. Murray, The Al−Mg (aluminum−magnesium) system, J. Phase Equilib. 3 (1982) 60–74, https://doi.org/10.1007/BF02873413.
[31] K. Liu, H. Yu, X. Li, S. Wu, Study on diffusion characteristics of Al-Cu systems and mechanical properties of intermetallics, J. Alloys Compd. 874 (2021) 159831, https://doi.org/10.1016/j.jallcom.2021.159831.
[32] Y. Guo, G. Liu, H. Jin, Intermetallic phase formation in diffusion-bonded Cu / Al laminates, J. Mater. Sci. 46 (2011) 2467–2473, https://doi.org/10.1007/s10853-010-5093-0.
[33] D. Kim, K. Kim, Interdiffusion and intermetallic compounds at Al/Cu interfaces in Al-50 vol.% Cu composite prepared by solid-state sintering, Materials 14 (2021) 4307, https://doi.org/10.3390/ma14154307.
[34] W. Liu, S. Zhang, F. Liu, H. Jin, M. Oezaslan, S. Ibrahim, Synthesis, characterization, and dealloying of Al- Cu alloys prepared using spark plasma sintering, IOP Conf. Series: Mater. Sci. Eng. 1249 (2022) 012033, https://doi.org/10.1088/1757-899X/1249/1/012033.
[35] M. Mukherjee, F. Garcia-Moreno, J. Banhart, Collapse of aluminum foam in two different atmospheres, Metall. Mater. Trans. B Process Metall. Mater. Process. Sci. 41 (2010) 500–504, https://doi.org/10.1007/s11663-010-9357-5.
[36] H.-M. Helwig, S. Hiller, F. Garcia-Moreno, J. Banhart, Influence of compaction conditions on the foamability of AlSi8Mg4 alloy, Metall. Mater. Trans. B Process Metall. Mater. Process. Sci. 40 (2009) 755–767, https://doi.org/10.1007/s11663-009-9264-9.
[37] F. García-Moreno, M. Mukherjee, C. Jiménez, J. Banhart, Pressure-induced foaming of metals, Jom 67 (2015) 955–965, https://doi.org/10.1007/s11837-015-1331-x.
[38] M.F. Ashby, A.G. Evans, N.A. Fleck, L.J. Gibson, J.W. Hutchinson, H.N. Wadley, Metal Foams: A Design Guide, Butterworth-Heinemann, 2000.
[39] M. Mukherjee, Evolution of Metal Foams during Solidification. https://api-depositonce.tu-berlin.de/server/api/core/bitstreams/2d581aff-d8a6-4639-b10c-49a177958546/content, 2009.
[40] D.M. Elzey, H.N.G. Wadley, The limits of solid state foaming, Acta Mater. 49 (2001) 849–859, https://doi.org/10.1016/S1359-6454(00)00395-5.
[41] B.M.A. Atwater, K.A. Darling, M.A. Tschopp, Towards reaching the theoretical limit of porosity in solid state metal foams: intraparticle expansion as a primary and additive means to create porosity, Adv. Eng. Mater. 16 (2014) 190–195, https://doi.org/10.1002/adem.201300431.
[42] J. Lázaro, E. Solórzano, J.A. De Saja, M.A. Rodríguez-Pérez, Early anisotropic expansion of aluminium foam precursors, J. Mater. Sci. 48 (2013) 5036–5046, https://doi.org/10.1007/s10853-013-7291-z.
[43] J. Lázaro, E. Laguna-gutiérrez, E. Solórzano, M.A. Rodríguez-Pérez, Effect of microstructural anisotropy of PM precursors on the characteristic expansion of aluminum foams, Metall. Mater. Trans. B Process Metall. Mater. Process. Sci. 44B (2013) 984–991, https://doi.org/10.1007/s11663-013-9852-6.